A Sensitivity Analysis of Satellite Navigation Using Landmarks

Evan M. Ward
U.S. Naval Research Lab
4555 Overlook Ave SW
Washington, DC 20375
evan.ward@nrl.navy.mil

Abstract—**This work evaluates the sensitivity of satellite orbit determination using known landmarks to orbital altitude and imaging geometry. Known landmark-based orbit determination is an autonomous navigation technique that uses a satellite's optical observatory to image known landmarks. Measurements for orbit determination are generated by using image processing algorithms to find the location of known landmarks in each image. Previous work stretching back to the Apollo Program has shown landmark navigation to be feasible and evaluated its sensitivity to lighting, inclination, pointing accuracy, image resolution, and number of images collected. Evaluating sensitivity to altitude and imaging geometry is useful for selecting an orbit for the satellite and for tasking the satellite in order to maximize the information gained from each collected image. First, a kinematic solution is studied to understand sensitivity when only a minimum amount of data are available, for example in an initial orbit determination. Separate solutions are found for small and large Field of View (FoV) observatories. For the small FoV case results show images near nadir are ideal. For the large FoV case results show that geometrical diversity is important when data are limited. Specifically there is a trade-off between minimizing the ground resolved distance and maximizing the angle between images from the satellite's perspective. Second, a batch weighted least squares covariance analysis is performed over a day with hundreds of measurements. Results show that when data are abundant imaging landmarks closer to nadir and from lower altitude produces more accurate orbit solutions for a given observatory. These conditions minimize the ground resolved distance and provide the most information about the in-track position of the satellite, typically the most uncertain coordinate. This work is a step towards fully autonomous satellite navigation and provides useful information for those designing image processing algorithms as well as satellite missions.**

TABLE OF CONTENTS

1. INTRODUCTION

Satellite navigation using landmarks enables autonomy from external navigation systems, which can reduce the burden on those systems and improve system reliability when faced with outages in external navigation systems [1]. In the early portion of the space age landmark navigation received significant attention from both NASA and the U.S. Air Force for Earth satellite navigation, but interest waned after the advent of the Navstar Global Positioning System. In the mean time landmark navigation became an important technology for deep space missions to other celestial bodies. More recently there has been renewed interested in landmark navigation of Earth satellites to increase satellite autonomy.

An early demonstration of spacecraft navigation with landmarks was the Apollo astronauts collecting bearing measurements to Earth and Moon landmarks using a space sextant [1]. In [2] Koso describes the measurement equations used on Apollo for sightings to known and unknown landmarks. A direction measurement to a known landmark constrains the vehicle to lie on a line. Repeated direction measurements to unknown landmarks during a pass can also be used to update the spacecraft's position and velocity. Using known landmarks provides better sensitivity for precise orbit determination and a better tie to the Earth fixed frame. Conversely using unknown landmarks does not require landmarks to be identified in various lighting conditions and it does not require a map or database of landmarks as it can use any visually distinctive feature.

In [3] Toda and Schlee build on the earlier work of Levine in [4], [5] to analyze navigation from tracking unknown landmarks. They show that the spacecraft state and landmark position is observable from measuring the direction to the landmark, though in some cases the observability is poor. They also show that unknown landmarks can be used without estimating their position by employing certain measurement differences. In [6] Paulson describes a new unknown landmark tracking system for the U.S. Air Force designed to measure the angular rate of landmarks as seen from the satellite, i.e. using image motion to navigate. The system would capture images at a high frame rate with a two dimensional Electro-Optical (EO) sensor and correlate subsequent images to find the shift across the sensor. Earth's rotation is used to measure latitude for polar orbiting satellites. Longitude can be measured coarsely if absolute time is known but precise longitude remains unobservable. Paulson also discusses using this system to update the vehicle's state between infrequent known landmark sightings. Paulson includes results from laboratory hardware in the loop tests to show such a system was feasible in 1972. For this system Kau describes the image correlation algorithm in [7].

In [8], White et al. perform a sensitivity analysis of using known landmarks for navigation with respect to the quantity of measurements as well as errors in the measurements and landmark location. Lowrie summarizes two different implementations of known landmark navigation techniques in [9]. The first attempts to correlate a known image chip with a collected image, searching the image pixel by pixel. Once a match is found Lowrie suggests interpolating between the pixels to find the sub-pixel location of the chip. The second

watches for linear features with optically distinct edges, such as roads or rivers, to cross the field of view and then measures the time the linear feature crossed the sensor's boresight. Markley, in [10], discusses how correlations between estimated attitude and orbit using known landmarks impact geolocation accuracy, that is the ability of the satellite to autonomously locate images that have no known landmarks in them. He shows that uncertainty in the estimated state tends to be highly correlated in a manner that cancels out to first order for geolocation. Markely also presents a non-singular formulation of the state that uses a quaternion for attitude and circular elements for orbit state. Chory et al. summarize autonomous navigation research up to 1984 in [11].

Autonomous landmark navigation is especially important to deep space missions that need to navigate near another body, such as for rendezvous with an asteroid. In [12], [13] Cheng et al. describe such a system that uses crater detection in images for proximity operations near the asteroid Eros. They describe it as an advance over operations for the Near Earth Asteroid Rendezvous mission where images were transmitted back to Earth for people to identify craters. In [14] Ma and Xu describe a similar method for the Japanese Hayabusa mission and show observability of the system. In [15] Lorenz et al. describe the autonomous landmark navigation system for the OSIRIS-REx mission to return a sample from an asteroid. The system uses an onboard database of features to render predicted images for the expected sun angle and viewing geometry that are then compared to images captured from the navigation cameras using cross correlation. In [16] Borschart et al. describe the success of the Deep Space 1 mission in demonstrating autonomous optical navigation for two months using observations of asteroids and go on to present an error analysis of optical navigation using asteroids throughout the solar system.

In more recent work on Earth satellite navigation using landmarks, Straub and Christian propose using multi-spectral imagery, such as is generated by Landsat, for coastline detection [17]. They show the system to be feasible for coarse accuracy, which is likely limited by the size of the objects that Landsat can resolve. Li et al. extend the analysis in [18] to evaluate sensitivity to lighting constraints and cloud cover. In [19] Zhang et al. show the feasibility of using small star trackers for landmark navigation using absolute and relative observations, similar to those proposed by [20]. Li and Xu, in [21], consider autonomous landmark navigation based on regular geometric shapes, e.g. ellipse and parallelogram, considering these to be common in imagery of cities. They compared a Kalman filter estimator with a computer vision algorithm designed for mobile ground robots and found the Kalman Filter to be far superior. They also evaluated the effects of lighting and clouds on the accuracy of the solution. In [22] Xu et al. consider placing the satellite observatory on a gimbal for greater access to geographically dispersed landmarks. They show the system is observable when the landmark is not always at the sub-satellite point.

The existing published work lacks a sensitivity analysis of imaging geometry for Earth satellites which would inform tasking of which landmarks to collect. This work presents mathematical models for several landmark measurement types in Section 2, conducts an analytical analysis of sensitivity to geometry for a point-wise kinematic solution in Section 3, and then presents sensitivity results for orbit determination over several revolutions using least squares in Section 4.

2. MEASUREMENT TYPES

Consider a satellite with an optical observatory in orbit around Earth. The Earth-centered Earth-fixed frame is denoted E, the Earth-centered inertial frame by I, and the camera's frame by C. The transformation from E to I is given by

$$\boldsymbol{r}_I = \boldsymbol{R}_{E\to I}\boldsymbol{r}_E \tag{1}$$

where $\boldsymbol{r}_I$ is position in I, $\boldsymbol{r}_E$ is position in E, and $\boldsymbol{R}_{E\to I}$ is the rotation from E to I. The transformation to C is given by

$$\boldsymbol{r}_C = \boldsymbol{R}_{I\to C}\left(\boldsymbol{r}_I - \boldsymbol{r}_{c,I}\right) \tag{2}$$

where $\boldsymbol{r}_C$ is position in C and $\boldsymbol{r}_{c,I}$ is the position of the camera in the inertial frame. This equation is applied to landmark navigation by substituting the position of the landmark for $\boldsymbol{r}_I$.

Direction Measurement

A direction measurement to a known landmark is the unit vector pointing towards the landmark in C. That is, for a landmark l,

$$\boldsymbol{r}_{l,C} = \boldsymbol{R}_{I\to C}\left(\boldsymbol{R}_{E\to I}\boldsymbol{r}_{l,E} - \boldsymbol{r}_{c,I}\right) = \boldsymbol{R}_{I\to C}\boldsymbol{d}_{l,I} \tag{3}$$

where $\boldsymbol{r}_l$ is the position of the landmark and $\boldsymbol{d}_{l,I}$ is the direction from the satellite to the landmark in the inertial frame. Since the direction measurement does not include the range the measurement is the unit vector $\hat{\boldsymbol{r}}_{l,C}$. The rotation from inertial to camera frame, $\boldsymbol{R}_{I\to C}$, is measured by the satellite's attitude determination system using, for example, a star tracker and inertial measurement unit. Since the landmark is known the position of the landmark in E is assumed to be known. The rotation $\boldsymbol{R}_{E\to I}$ can be computed according to the procedure defined by the International Earth Rotation Service in [23]. This leaves $\boldsymbol{r}_{c,I}$, the position of the camera in the inertial frame, as the remaining unknown.

Differenced Direction Measurement

Consider a single image that contains two known landmarks. The measured directions may be differenced to remove the dependency on spacecraft attitude:

$$\sin\theta = |\hat{\boldsymbol{r}}_{l_1,C}\times\hat{\boldsymbol{r}}_{l_2,C}| \tag{4}$$

$$\sin\theta = |\boldsymbol{R}_{I\to C}|\left|\hat{\boldsymbol{d}}_{l_1,I}\times\hat{\boldsymbol{d}}_{l_2,I}\right| \tag{5}$$

$$\sin\theta = \left|\hat{\boldsymbol{d}}_{l_1,I}\times\hat{\boldsymbol{d}}_{l_2,I}\right| \tag{6}$$

where (6) shows that the measured angular distance, θ, only depends on the position of the satellite and landmarks at the measurement time. One drawback to this formulation is that two landmark observations are reduced to a single scalar equation, necessitating more observations before a state estimate can be formed.

3. KINEMATIC SOLUTION

In cases where the satellite does not have a priori knowledge of its location, such as initial orbit determination, it can be useful to determine the satellite's position from a minimum number of observations. For known landmark observations a minimum of two observations are required to estimate the camera's position. The following sections present the equations for determining position and analyze the sensitivity to measurement geometry first for a small Field of View (FoV) and then for a large FoV.

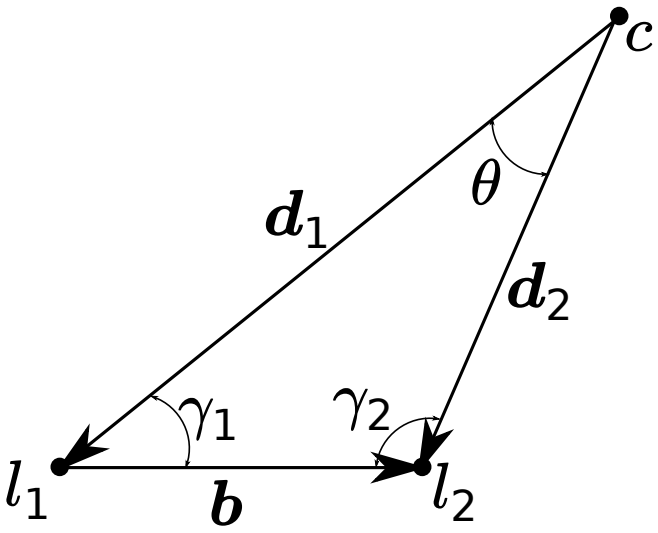

Figure 1: Diagram of a camera observing the direction to two landmarks.

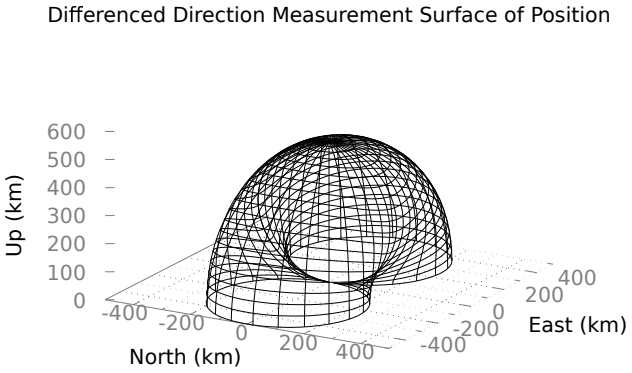

Figure 2: From a single direction difference measurement the satellite is constrained to be on the surface of a doughnut with the baseline at the center. In the example plotted here the baseline is 1 km and is aligned with the local meridian. The measured angular difference is $2\,\mathrm{mrad}$.

From a Small Image

The position of the spacecraft may be computed from a single image if two (or more) landmarks are present. The geometry for this scenario is shown in Figure 1. Let $\boldsymbol{b} = \boldsymbol{d}_{l_2,I} - \boldsymbol{d}_{l_1,I}$ be the baseline vector between the known landmarks. Substituting in to (6) gives

$$\sin\theta = \left|\hat{\boldsymbol{d}}_{l_1,I} \times \frac{\boldsymbol{d}_{l_1,I} + \boldsymbol{b}}{d_2}\right| \tag{7}$$

$$= \frac{\left|\hat{\boldsymbol{d}}_{l_1,I} \times \boldsymbol{b}\right|}{d_2} \tag{8}$$

$$= \frac{b}{d_2}\sin\gamma_1 \tag{9}$$

$$= \frac{b}{d_2}\sqrt{1-\cos^2\varepsilon\cos^2\alpha} \tag{10}$$

where γ is the angle between the baseline and the line of sight, and ε, α are the elevation and azimuth coordinates of the satellite, assuming without loss of generality that the baseline is aligned with the local North direction.[2] Assuming a small field of view ($\theta \ll 1$, $d \simeq d_1 \simeq d_2 \gg b$, and $\gamma \simeq \gamma_1 \simeq \gamma_2$) gives the equation of a surface in spherical coordinates.

$$d = \frac{b}{\theta}\sqrt{1-\cos^2\varepsilon\cos^2\alpha} \tag{11}$$

An example of the surface is shown in Figure 2, which is half a doughnut since we assume the satellite is above the landmark's local horizon.[3] The surface may be further reduced to a quarter of a doughnut if it can be determined from the image which end of the baseline is closer to the satellite. Two special cases are worth noting. First, when the baseline is orthogonal to the satellite's line of sight then the line of position is a circle centered on the baseline

$$d = \frac{b}{\theta} \tag{12}$$

which is a measurement of the range. Second, when the satellite lies in the plane defined by the baseline and its local vertical then the line of position is a circle resting on the baseline

$$d = \frac{b}{\theta}\sin\varepsilon \tag{13}$$

which is a range-like measurement when the satellite is near zenith.

Combining the direction difference measurement with a single direction measurement creates a line that intersects the doughnut at the position of the satellite. Rearranging (3) gives

$$\boldsymbol{r} = -d_l\hat{\boldsymbol{d}}_{l,I} \tag{14}$$

where d_l is the range from the landmark to the camera and $\boldsymbol{r}$ is the position of the camera relative to the landmark. Substituting (8), making the small field of view assumptions above, and dropping subscripts since all quantities are now in the inertial frame gives

$$\boldsymbol{r} = -\frac{\left|\hat{\boldsymbol{d}} \times \boldsymbol{b}\right|}{\theta}\hat{\boldsymbol{d}} = -\frac{b\sin\gamma}{\theta}\hat{\boldsymbol{d}} \tag{15}$$

which is the position of the camera in terms of measured quantities.

Now, the focus turns to an error analysis to determine the expected error in position for given measurement errors and to determine the ideal viewing angles from the satellite for making an observation. Consider that the measured direction vector $\hat{\boldsymbol{d}}$ is perturbed by two small rotations each about an axis perpendicular to $\hat{\boldsymbol{d}}$. The axes are selected so that one is in the plane containing the landmarks and camera while the

[2] If the baseline is not so aligned the offset is subtracted from α, which is simply a rotation about zenith.

[3] Though some landmarks may be visible from below the horizon due to refraction or their height they are not expected to be useful due to the atmospheric distortion at low elevation angles.

other is normal to it. The axes are

$$\hat{\boldsymbol{n}}_1 = \frac{\hat{\boldsymbol{d}} \times \hat{\boldsymbol{b}}}{\left|\hat{\boldsymbol{d}} \times \hat{\boldsymbol{b}}\right|} = \frac{\hat{\boldsymbol{d}} \times \hat{\boldsymbol{b}}}{\sin\gamma} \tag{16}$$

$$\hat{\boldsymbol{n}}_2 = \hat{\boldsymbol{d}} \times \hat{\boldsymbol{n}}_1 \tag{17}$$

$$\tag{18}$$

which defines an orthonormal reference system. The small error rotation about the axis is

$$\boldsymbol{R}_{\hat{\boldsymbol{n}}}(\phi) = (1 + \phi\hat{\boldsymbol{n}}\times) \tag{19}$$

with only a small abuse of notation. Therefore the perturbed direction is

$$\hat{\boldsymbol{d}}_p = \boldsymbol{R}_{\hat{\boldsymbol{n}}_1}(\phi_1)\, \boldsymbol{R}_{\hat{\boldsymbol{n}}_2}(\phi_2)\, \hat{\boldsymbol{d}} \tag{20}$$

$$= \hat{\boldsymbol{d}} + \phi_1\hat{\boldsymbol{n}}_1 \times \hat{\boldsymbol{d}} + \phi_2\hat{\boldsymbol{n}}_2 \times \hat{\boldsymbol{d}} \tag{21}$$

$$= \hat{\boldsymbol{d}} - \phi_1\hat{\boldsymbol{n}}_2 + \phi_2\hat{\boldsymbol{n}}_1 \tag{22}$$

where ϕ_1 and ϕ_2 are two small independent angular errors. As shown in [24], small angular perturbations are equivalent to small perturbations in the tangent plane. Substituting (22) into (15) gives

$$\boldsymbol{r}_p = -\frac{\left|\hat{\boldsymbol{d}}_p \times \boldsymbol{b}\right|}{\theta}\hat{\boldsymbol{d}}_p \tag{23}$$

Then derivatives are taken with respect to the three angular measurement errors:

$$\frac{\partial \boldsymbol{r}_p}{\partial\theta} = \frac{\left|\hat{\boldsymbol{d}}_p \times \boldsymbol{b}\right|}{\theta^2}\hat{\boldsymbol{d}}_p = -\frac{\boldsymbol{r}_p}{\theta} \simeq -\frac{r}{\theta}\hat{\boldsymbol{d}} \tag{24}$$

$$\frac{\partial \boldsymbol{r}_p}{\partial\phi_1} = -\frac{1}{\theta}\left(\frac{\partial\hat{\boldsymbol{d}}_p}{\partial\phi_1}\left|\hat{\boldsymbol{d}}_p \times \boldsymbol{b}\right| + \hat{\boldsymbol{d}}_p\frac{\partial\left|\hat{\boldsymbol{d}}_p \times \boldsymbol{b}\right|}{\partial\phi_1}\right) \tag{25}$$

$$= -\frac{1}{\theta}\left(-\hat{\boldsymbol{n}}_2\left|\hat{\boldsymbol{d}}_p \times \boldsymbol{b}\right| + \hat{\boldsymbol{d}}_p\frac{\hat{\boldsymbol{d}}_p \times \boldsymbol{b}}{\left|\hat{\boldsymbol{d}}_p \times \boldsymbol{b}\right|} \cdot \frac{\partial\hat{\boldsymbol{d}}_p \times \boldsymbol{b}}{\partial\phi_1}\right) \tag{26}$$

$$\simeq -\frac{1}{\theta}\left(-\hat{\boldsymbol{n}}_2 b\sin\gamma + \hat{\boldsymbol{d}}\left(\hat{\boldsymbol{n}}_1 \cdot (-b\cos\gamma\hat{\boldsymbol{n}}_1)\right)\right) \tag{27}$$

$$= \frac{1}{\theta}\left(\hat{\boldsymbol{n}}_2 b\sin\gamma + \hat{\boldsymbol{d}}\, b\cos\gamma\right) \tag{28}$$

$$= r\left(\hat{\boldsymbol{n}}_2 + \hat{\boldsymbol{d}}\cot\gamma\right) \tag{29}$$

$$\frac{\partial \boldsymbol{r}}{\partial\phi_2} = -\frac{1}{\theta}\left(\frac{\partial\hat{\boldsymbol{d}}_p}{\partial\phi_2}\left|\hat{\boldsymbol{d}}_p \times \boldsymbol{b}\right| + \hat{\boldsymbol{d}}_p\frac{\partial\left|\hat{\boldsymbol{d}}_p \times \boldsymbol{b}\right|}{\partial\phi_2}\right) \tag{30}$$

$$\simeq -\frac{1}{\theta}\left(\hat{\boldsymbol{n}}_1\left|\hat{\boldsymbol{d}} \times \boldsymbol{b}\right| + \hat{\boldsymbol{d}}\left(\hat{\boldsymbol{n}}_1 \cdot \left(-\sin\gamma\hat{\boldsymbol{d}} - \cos\gamma\hat{\boldsymbol{n}}_2\right)\right)\right) \tag{31}$$

$$= -\hat{\boldsymbol{n}}_1\frac{\left|\hat{\boldsymbol{d}} \times \boldsymbol{b}\right|}{\theta} \tag{32}$$

$$= -r\hat{\boldsymbol{n}}_1 \tag{33}$$

$$\tag{34}$$

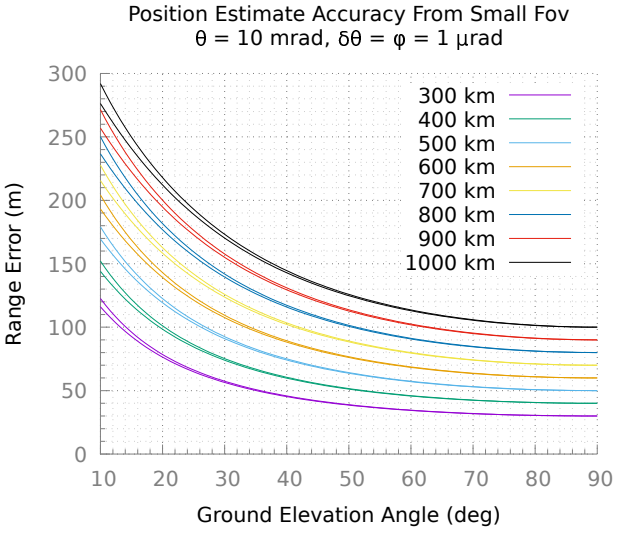

Figure 3: Illustrative example of range error as a function of imaging geometry for several satellite altitudes. The lower curve of each pair corresponds to when the line of sight is perpendicular to the baseline ($\alpha = \gamma = \frac{\pi}{2}$). The upper curve corresponds to $\alpha = 0$, which is the minimum value of γ, i.e. $\gamma = \varepsilon$.

assuming that γ is not small. (I.e. the camera is not co-linear with the baseline.) Thus the error in the computed position is

$$\delta\boldsymbol{r} = \frac{\partial\boldsymbol{r}}{\partial\theta}\delta\theta + \frac{\partial\boldsymbol{r}}{\partial\phi_1}\phi_1 + \frac{\partial\boldsymbol{r}}{\partial\phi_1}\phi_2 \tag{35}$$

$$= r\left(\left(\frac{\delta\theta}{\theta} + \phi_1\cot\gamma\right)\hat{\boldsymbol{d}} - \phi_2\hat{\boldsymbol{n}}_1 + \phi_1\hat{\boldsymbol{n}}_2\right) \tag{36}$$

$$|\delta\boldsymbol{r}| = r\sqrt{\left(\frac{\delta\theta}{\theta} + \phi_1\cot\gamma\right)^2 + \phi_2^2 + \phi_1^2} \tag{37}$$

which permits several insights. First, the position error is proportional to the range. Second, in the directions normal to the line of sight the position error is simply the angular error multiplied by the range, as one might expect. Third, the error in range can be minimized when the angular size of the baseline, θ, is large and when the line of sight is perpendicular to the baseline ($\gamma = \frac{\pi}{2}$). Fourth, when the line of sight is not nearly co-linear with the baseline (which is likely impractical) the $\frac{\delta\theta}{\theta}$ term dominates because it is the division of two small quantities whereas the other terms are just small quantities. Therefore

$$|\delta\boldsymbol{r}| \simeq r\frac{\delta\theta}{\theta} \tag{38}$$

which indicates the percent error in range is the percent error in measuring θ. Figure 3 plots the range error from (37) as a function of elevation angle when the line of sight is perpendicular to the baseline ($\gamma = \frac{\pi}{2}$) as well as when the line of sight is above the baseline ($\gamma = \varepsilon$). In the figure θ is assumed to be constant, i.e. proportional to the camera's field of view. If on the other hand the length of the baseline is assumed to be constant then the error is given by (39) which shows that errors are larger at lower elevation angles than

in (38).

$$\delta \boldsymbol{r} = r\left(\left(\frac{r}{b\sin\gamma}\delta\theta + \phi_1\cot\gamma\right)\hat{\boldsymbol{d}} - \phi_2\hat{\boldsymbol{n}}_1 + \phi_1\hat{\boldsymbol{n}}_2\right) \tag{39}$$

From a Large Image

This section considers the case of determining the position of a camera with a large field of view, or equivalently two co-located small field of view cameras with a large angle separating their boresight. Again, the geometry is shown in Figure 1. The baseline and unit direction vectors are known and therefore all of the angles are known. The position of the camera is found by solving for the range from the landmarks.

Using the law of sines, the range to the first landmark is

$$d_1 = \frac{b\sin\gamma_2}{\sin\theta} \tag{40}$$

therefore the position of the camera is

$$\boldsymbol{r}_c = \boldsymbol{r}_{l_1} - d_1\hat{\boldsymbol{d}}_1 \tag{41}$$

and similarly for the other landmark.

Now consider small angular perturbations about the axis $\hat{\boldsymbol{n}}_1 = \boldsymbol{d}_1 \times \boldsymbol{b}$ by ϕ_1 and ϕ_2 to the measured directions $\hat{\boldsymbol{d}}_1$ and $\hat{\boldsymbol{d}}_2$, respectively. The perturbed angles are then

$$\sin\theta_p = \sin\theta + (\phi_2 - \phi_1)\cos\theta \tag{42}$$

and

$$\sin\gamma_{2p} = \sin\gamma_2 - \phi_2\cos\gamma_2 \tag{43}$$

The perturbed range is

$$d_{1p} = \frac{b\sin\gamma_{2p}}{\sin\theta_p} \tag{44}$$

$$= b\frac{\sin\gamma_2 - \phi_2\cos\gamma_2}{\sin\theta + (\phi_2 - \phi_1)\cos\theta} \tag{45}$$

and its derivatives are

$$\frac{\partial d_{1p}}{\partial\phi_1} = d_{1p}\frac{\cos\theta}{\sin\theta + (\phi_2 - \phi_1)\cos\theta} \tag{46}$$

$$\simeq d_1\cot\theta \tag{47}$$

$$\frac{\partial d_{1p}}{\partial\phi_2} = \frac{b}{\left(\sin\theta + (\phi_2 - \phi_1)\cos\theta\right)^2}\cdot \left(-\left(\sin\theta + (\phi_2 - \phi_1)\cos\theta\right)\cos\gamma_2 - \left(\sin\gamma_2 - \phi_2\cos\gamma_2\right)\cos\theta\right) \tag{48}$$

$$\simeq -b\frac{\sin\left(\theta + \gamma_2\right)}{\sin^2\theta} \tag{49}$$

$$= -b\frac{\sin\gamma_1}{\sin^2\theta} \tag{50}$$

$$= -\frac{d_2}{\sin\theta} \tag{51}$$

From these formulas it is clear the magnitude of the errors decrease as the ranges decrease and as θ approaches $\frac{\pi}{2}$. It is also clear the system is unobservable at $\theta = 0$ as may be expected. The perturbed position and its derivatives are

$$\boldsymbol{r}_{cp} = \boldsymbol{r}_{l_1} - d_{1p}\hat{\boldsymbol{d}}_{1p} \tag{52}$$

$$\frac{\partial\boldsymbol{r}_{cp}}{\partial\phi_1} = -d_{1p}\hat{\boldsymbol{n}}_2 - \hat{\boldsymbol{d}}_{1p}\frac{\partial d_{1p}}{\partial\phi_1} \tag{53}$$

$$\simeq -d_1\left(\hat{\boldsymbol{n}}_2 + \cot\theta\hat{\boldsymbol{d}}_1\right) \tag{54}$$

$$\frac{\partial\boldsymbol{r}_{cp}}{\partial\phi_2} = -\hat{\boldsymbol{d}}_{1p}\frac{\partial d_{1p}}{\partial\phi_2} \tag{55}$$

$$\simeq d_2\csc\theta\hat{\boldsymbol{d}}_1 \tag{56}$$

where $\hat{\boldsymbol{n}}_2$ is perpendicular to $\hat{\boldsymbol{d}}_1$ and $\hat{\boldsymbol{n}}_1$.

Now assume $d = d_1 = d_2$ which minimizes the range for a given θ, both landmarks are on the surface of a spherical Earth with radius $r_\oplus$, and the camera is outside the Earth. Further assume that ϕ_1 and ϕ_2 are independent and identically distributed Gaussian random variables with standard deviation σ_ϕ. Then for in plane errors the ratio of position to measurement errors is

$$\frac{\sigma_{\boldsymbol{r}_c}}{\sigma_\phi} = \sqrt{\frac{d^2}{\sin^2\theta} + \frac{d^2\cos^2\theta}{\sin^2\theta} + d^2} \tag{57}$$

$$= \sqrt{2}d\csc\theta \tag{58}$$

The out of plane errors are proportional d and the estimated out of plane position is the average of the out of plane errors in $\hat{\boldsymbol{d}}_1$ and $\hat{\boldsymbol{d}}_2$. Thus the ratio of position to measurement errors is

$$\frac{\sigma_{\boldsymbol{r}_c}}{\sigma_\phi} = d\sqrt{2\csc^2\theta + \frac{1}{2}} \tag{59}$$

which shows in plane errors are always greater than out of plane errors for this viewing geometry. Equation 59 is equivalent to [16, eq. (10)] under the assumption of equal range to the two targets.

Equation 58 and (59) are plotted together in Figure 4 as a function of elevation angle and in Figure 5 as a function of nadir angle. In each figure the upper curve for each altitude corresponds to (59) and the lower curve corresponds to (58). For the altitudes considered there is a fairly flat minimum between 40° and 60° Ground Elevation Angle (GEA), which corresponds to the same minimum between 30° and 40° off nadir. Considering out of plane errors slightly shifts the minimum towards smaller θ where d is smaller. Errors increase for low elevation angles due to increasing range and Earth's curvature. Errors increase for large elevation angles due to decreasing baseline length. For two landmarks near nadir the large field of view case degenerates to the small field of view case presented above in (37) and Figure 3.

4. SIMULATION

During steady state operation of the satellite many observations are available over a longer time span. This section investigates the error characteristics and sensitivities of steady state orbit determination using a batch weighted least squares covariance analysis with simulated measurements. Direction measurements are modeled using the method described

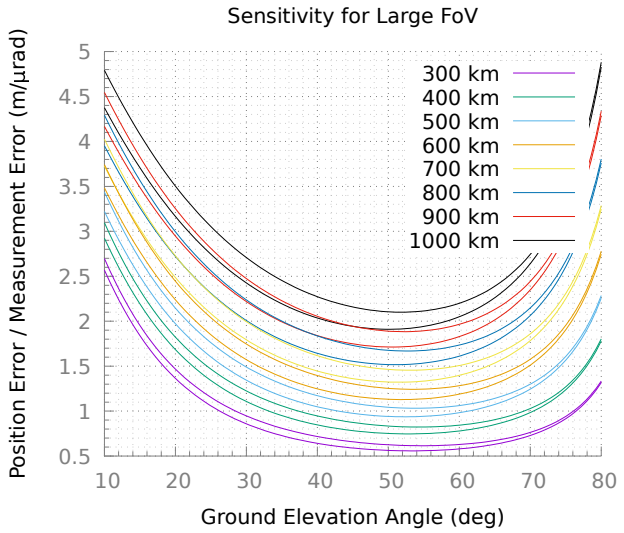

Figure 4: Plot of position errors as a function of GEA for a large FoV.

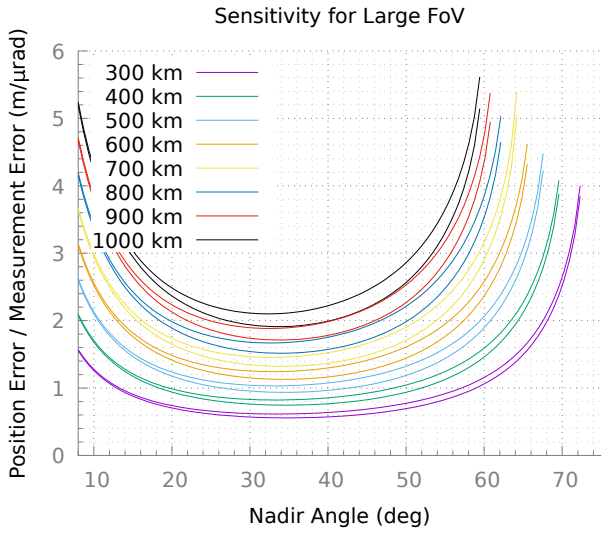

Figure 5: Plot of position errors as a function of nadir angle for a large FoV.

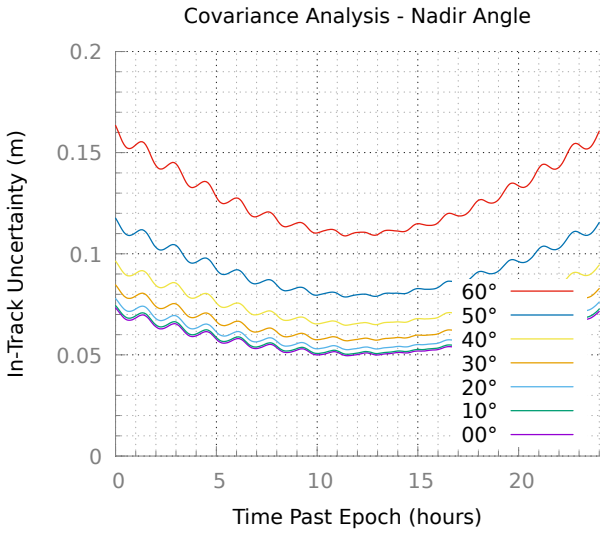

(a) Estimated in-track standard deviation.

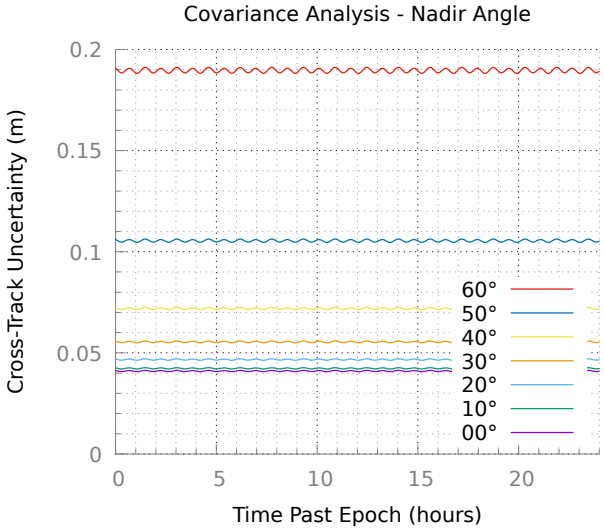

(b) Estimated cross-track standard deviation.

Figure 6: Covariance analysis results of varying nadir angle to landmark.

in [25]. The Orekit open-source astrodynamics library is used to perform the simulations.[4]

A satellite is simulated for one day in a nominal $500\,\mathrm{km}$ circular orbit. It is assumed that the only force acting on the satellite is Earth gravity, modeled to degree and order six. Twenty times each orbit a pair of measurements to landmarks are collected at equal angles off nadir, one to port and the other to starboard, for a total of 286 measurements per day. The nadir angle is varied from one run to the next. Measurements are generated regardless of practical constraints such as land, lighting, and weather. Each direction observation is assumed to be an independent sample from a Gaussian distribution with standard deviation $1\,\mu\mathrm{rad}$. No covariance consider parameters are included. This will produce an optimistic estimate of the covariance, but it is still useful for gauging the relative effect of measurement uncertainty when varying parameters.

Figure 6 shows the estimated in-track and cross-track covariance during the fit span. Figure 7 shows the estimated uncertainty as a function of nadir angle. From these plots it is clear images near nadir minimize estimate uncertainty. Since errors are proportional to $r\phi$ it is consistent that the minimum range geometry would produce the lowest estimate error. In Figure 7 for small nadir angles the in-track uncertainty is the largest component, as is typical for orbit determination, but the cross-track uncertainty grows more quickly with the two becoming equal near $41°$ off nadir. This characteristic is likely explained by the size of a pixel projected to the ground. When imaging to port or starboard the in-track dimension grows with the range whereas the cross-track direction also grows because the Earth slopes away from the line of sight.

[4] `https://orekit.org`

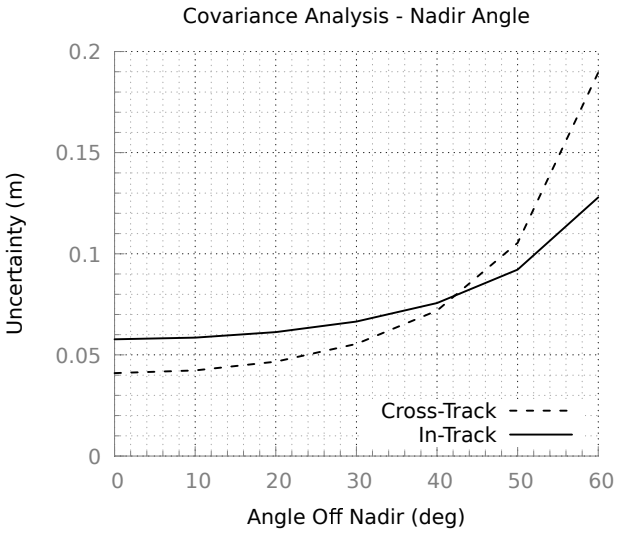

Figure 7: Estimated uncertainty in the in-track and cross-track directions as a function of nadir angle to the landmarks.

To characterize the variation of uncertainty with altitude the above experiment is repeated while holding the nadir angle constant at zero and varying altitude from $300\,\mathrm{km}$ to $1100\,\mathrm{km}$. The estimated uncertainty is shown in Figure 8 and in Figure 9 as a function of orbit altitude. Again it appears that range, or equivalently the projected size of a pixel, is the primary factor in determining the uncertainty. This result is consistent with those from Section 3 where increasing altitude is seen to produce proportional increases in uncertainty.

5. Conclusions

In conclusion the ideal imaging geometry is determined for three cases of using known landmark measurements. When determining position from a single small image it should be taken near nadir. When determining position from a single large image, or two small images, the ideal geometry varies with orbital altitude, but is near 35° off nadir in low Earth orbit. When determining an orbit from many measurements the images should be collected near nadir. Additionally decreasing the altitude decreases the uncertainty proportionally in all cases. These results provide useful input for satellite mission design and for observatory tasking so that the information gained from collected measurements can be maximized.

Future work includes analyzing differenced measurements of the same landmark at different times, producing a measurement sensitive to velocity. Furthermore the scope of steady state orbit determination analysis could be expanded by including consider parameters, refraction, and varying parameters simultaneously for a more global sensitivity analysis. While the current work establishes ideal imaging geometries for one, two, or many images, future work could establish the ideal imaging geometry as a function of the number of images collected to bridge the gap between initial and steady state orbit determination. Though much remains to be done, this is a step towards fully autonomous satellite navigation.

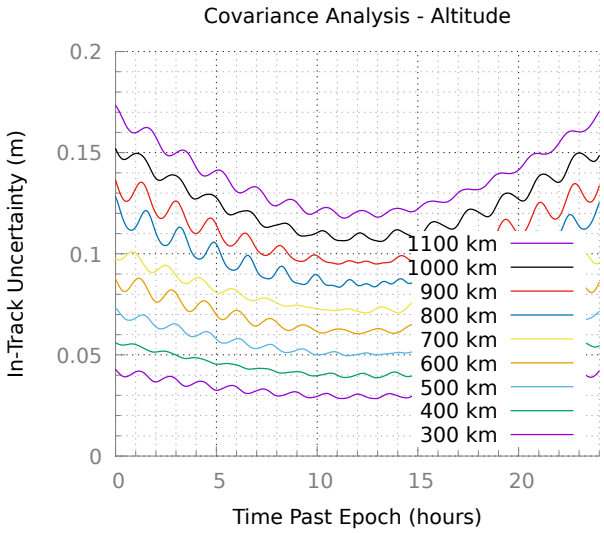

(a) Estimated in-track standard deviation.

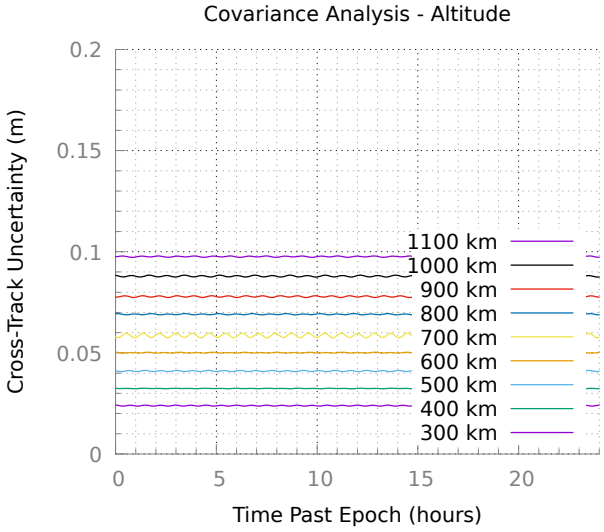

(b) Estimated cross-track standard deviation.

Figure 8: Covariance analysis results of varying orbital altitude.

Acknowledgments

The author gratefully acknowledges Dr. Bryan Brown for his thorough review and the U.S. Naval Research Lab their support.

References

[1] D. G. Hoag, "The navigation, guidance and control of a manned lunar landing," in *Space Navigation Guidance and Control*, C. Draper, W. Wrigley, G. Hoag, R. H. Battin, J. E. Miller, D. A. Koso, A. L. Hopkins, and W. E. V. Velde, Eds. Cambridge, MA: Massachusetts Institutde of Technology Instrumentation Laboratory, Jun. 1965, vol. 1, no. R-500, pp. II1–II92.

[2] D. A. Koso, "Optical measurements and navigation phenomena," in *Space Navigation Guidance and Con-*

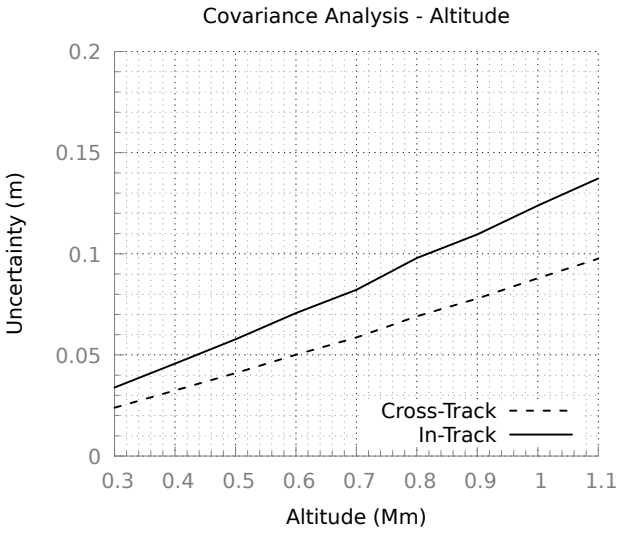

Figure 9: Estimated uncertainty in the in-track and cross-track directions as a function of altitude.

trol, C. Draper, W. Wrigley, G. Hoag, R. H. Battin, J. E. Miller, D. A. Koso, A. L. Hopkins, and W. E. V. Velde, Eds. Cambridge, MA: Massachusetts Institudte of Technology Instrumentation Laboratory, Jun. 1965, vol. 2, no. R-500, pp. V1–V45.

[3] N. F. Toda and F. H. Schlee, "Autonomous orbital navigation by optical tracking of unknown landmarks." *Journal of Spacecraft and Rockets*, vol. 4, no. 12, pp. 1644–1648, Dec. 1967.

[4] G. Levine, "A method or orbital navigation using optical sightings to unknown landmarks," in *Guidance Control Conference*, Minneapolis, MN, Aug. 1965. [Online]. Available: https://doi.org/10.2514/6.1965-1226

[5] G. M. Levine, "A method of orbital navigation using optical sightings to unknown landmarks." *AIAA Journal*, vol. 4, no. 11, pp. 1928–1931, 1966. [Online]. Available: https://doi.org/10.2514/3.3820

[6] D. Paulson, "Autonomous satellite navigation from strapdown landmark measurement," in *3rd Symposium on Nonlinear Estimation Theory*, San Diego, CA, Sep. 1972.

[7] S. P. Kau and D. C. Paulson, "Sensor concept and algorithms for a completely strapdown autonomous navigation approach," *Joint Automatic Control Conference*, vol. 11, pp. 643 – 644, 1973.

[8] R. L. White, M. B. Adams, E. G. Geisler, and F. D. Grant, "Attitude and oribit estimation using stars and landmarks," *IEEE Transactions on Aerospace and Electronic Systems*, vol. AES-11, no. 2, pp. 195–203, 1975.

[9] J. Lowrie, "Autonomous navigation systems technology assessment," in *17th Aerospace Sciences Meeting*, New Orleans, LA, Jan. 1979. [Online]. Available: https://doi.org/10.2514/6.1979-56

[10] F. L. Markley, "Autonomous satellite navigation using landmarks," in *AAS/AIAA Astrodynamics Conference*, North Lake Tahoe, NV, 1981, pp. 989–1010.

[11] M. Chory, D. Hoffman, C. Major, and V. Spector, "Autonomous navigation - where we are in 1984," in *AIAA Guidance and Control Conference*, Seattle, WA, Aug. 1984, pp. 27–37. [Online]. Available: https:/doi.org/10.2514/6.1984-1826

[12] Y. Cheng and J. K. Miller, "Autonomous landmark based spacecraft navigation system," in *AAS/AIAA Astrodynamics Specialist Conference*, Ponce, Puerto Rico, 2003.

[13] Y. Cheng, A. E. Johnson, L. H. Matthies, and C. F. Olson, "Optical landmark detection for spacecraft navigation," in *AAS/AIAA Astrodynamics Specialist Conference*, Ponce, Puerto Rico, 2003.

[14] H. Ma and S. Xu, "Only feature point line-of-sight relative navigation in asteroid exploration descent stage," *Aerospace Science and Technology*, vol. 39, p. 628, 2014.

[15] D. A. Lorenz, R. Olds, A. May, C. Mario, M. E. Perry, E. E. Palmer, and M. Daly, "Lessons learned from OSIRIS-REx autonomous navigation using natural feature tracking," in *2017 IEEE Aerospace Conference*, 2017, pp. 1–12.

[16] S. B. Broschart, N. Bradley, and S. Bhaskaran, "Kinematic approximation of position accuracy achieved using optical observations of distant asteroids," *Journal of Spacecraft and Rockets*, vol. 56, no. 5, pp. 1383–1392, 2019. [Online]. Available: https://doi.org/10.2514/1.A34354

[17] M. Straub and J. A. Christian, "Autonomous optical navigation for earth-observing satellites using coastline matching," in *AIAA Guidance, Navigation, and Control Conference*, 2015.

[18] M. Li, B. Xu, and L. Zhang, "Orbit determination for remote-sensing satellites using only optical imagery," *International Journal of Remote Sensing*, vol. 38, no. 5, pp. 1350–1364, Mar. 2017.

[19] H. Zhang, L. Kazemi, and J. Enright, "Landmark-based optical navigation using nanosatellite star trackers," in *2017 IEEE Aerospace Conference*, 2017.

[20] K. Janschek and S. Dyblenko, "Satellite autonomous navigation based on image motion analysis," *IFAC Proceedings Volumes*, vol. 34, no. 15, p. 111, 2001.

[21] M. Li and B. Xu, "Autonomous orbit and attitude determination for earth satellites using images of regular-shaped ground objects," *Aerospace Science and Technology*, vol. 80, p. 192, 2018.

[22] C. Xu, X. Huang, M. Li, and D. Wang, "Autonomous navigation using natural landmark measurements for earth orbit satellites," in *2019 Chinese Control Conference (CCC)*, Jul. 2019, pp. 4078–4082.

[23] "IERS conventions (2010)," Gérard Petit and Brian Luzum, Eds., Frankfurt am Main: Verlag des Bundesamts für Kartographie und Geodäsie, IERS Technical Note 36, 2010.

[24] M. D. Shuster, "Maximum likelihood estimation of spacecraft attitude," *Journal of the Astronautical Sciences*, vol. 37, no. 1, pp. 79–88, Jan. 1989. [Online]. Available: http://malcolmdshuster.com/Pub_1989b_J_MLE_scan.pdf

[25] E. M. Ward and G. Carbott, "On directional measurement representation in orbit determination," in *AIAA/AAS Astrodynamics Specialist Conference*, Sep. 2016.

BIOGRAPHY

Evan M. Ward *received his B.S. in Aerospace Engineering from Penn State and his M.S. in Computer Science from Johns Hopkins. He currently works in the Astrodynamics and Navigation Section at the U.S. Naval Research Lab in DC. His interests include autonomous navigation, geolocation, and orbit determination. He currently leads development of the Orbit Covariance Estimation and Analysis (OCEAN) software and serves on the Project Management Committee for the Orekit open source astrodynamics library.*